LETTERS
PUBLISHED ONLINE: 27 NOVEMBER 2011 | DOI: 10.1038/NPHYS2149
nature physics

Coherent control of three-spin states in a triple quantum dot

L. Gaudreau[1,2†], G. Granger[1†], A. Kam[1], G. C. Aers[1], S. A. Studenikin[1], P. Zawadzki[1], M. Pioro-Ladrière[2], Z. R. Wasilewski[1] and A. S. Sachrajda[1*]

Spin qubits involving individual spins in single quantum dots or coupled spins in double quantum dots have emerged as potential building blocks for quantum information processing applications[1–4]. It has been suggested that triple quantum dots may provide additional tools and functionalities. These include encoding information either to obtain protection from decoherence or to permit all-electrical operation[5], efficient spin busing across a quantum circuit[6], and to enable quantum error correction using the three-spin Greenberger-Horn-Zeilinger quantum state. Towards these goals we demonstrate coherent manipulation of two interacting three-spin states. We employ the Landau–Zener–Stückelberg[7,8] approach for creating and manipulating coherent superpositions of quantum states[9]. We confirm that we are able to maintain coherence when decreasing the exchange coupling of one spin with another while simultaneously increasing its coupling with the third. Such control of pairwise exchange is a requirement of most spin qubit architectures[10], but has not been previously demonstrated.

Following the spin qubit proposal by Loss and DiVincenzo[10] and the electrostatic isolation of single spins in quantum dots (QDs)[11] and double quantum dots (DQDs)[12], coherent manipulation was demonstrated in two-level systems based on single-spin up and down states[2] as well as two-spin singlet and triplet states[1]. Here we demonstrate coherent manipulation of a two-level system based on three-spin states. We employ the triple quantum dot (TQD) device layout shown in Fig. 1a, consisting of multiple metallic gates on a GaAs/AlGaAs heterostructure. The gates are used to electrostatically define three QDs in series within a two-dimensional electron gas 110 nm below the surface. The QDs are surrounded by two quantum point contact charge detectors (QPCs)[13]. The QPC conductance identifies the number of electrons in each QD and its derivative with respect to a relevant gate voltage maps out the device configuration stability diagram. We tune the device to the qubit operating electronic configuration, $(N_L, N_C, N_R) = (1,1,1)$, between two spin-to-charge conversion regimes (1,0,2) and (2,0,1), where L, C and R refer to the left, centre and right QDs respectively. The detuning, ε, controls the energy difference between configurations (1,0,2), (1,1,1) and (2,0,1). The exchange coupling, J, depends on ε and the tunnel couplings.

In this paper we concentrate on two scenarios. In the first scenario, at each point in the stability diagram the exchange coupling to the centre spin from one or both of the edge spins is minimal (that is, one edge spin resembles a passive spectator). This configuration is used as a control to confirm that our device maps onto two-spin results in this limit[9]. In the second scenario a true three-interacting-spin regime is achieved. (Results from a third intermediate regime are shown in the Supplementary Information.)

The energy level spectrum of a TQD (ref. 14) consists of quadruplets Q with total spin $S = 3/2$ separated by the Zeeman energy in a magnetic field and doublets Δ' and Δ with $S = 1/2$. The two states of our qubit consist of one of the quadruplets, $Q_{3/2}$, and one of the doublets, $\Delta'_{1/2}$, where

$$|Q_{3/2}\rangle = |\uparrow\uparrow\uparrow\rangle$$

$$|\Delta'_{1/2}\rangle = \frac{(-J_{LC}+J_{RC}+\Omega)|\uparrow\uparrow\downarrow\rangle-(J_{RC}+\Omega)|\uparrow\downarrow\uparrow\rangle+J_{LC}|\downarrow\uparrow\uparrow\rangle}{\sqrt{4\Omega^2+2\Omega(2J_{RC}-J_{LC})}}$$

with $\Omega = \sqrt{J_{LC}^2+J_{RC}^2-J_{LC}J_{RC}}$, and where J_{LC} (J_{RC}) is the exchange coupling between the left (right) and centre spins. (Other three-spin states are described in more detail in the Supplementary Information.)

Figure 1b illustrates the three-spin energy spectrum as a function of detuning (zero detuning is defined as the centre of the (1,1,1) regime as shown). Experimentally we can tune the (1,1,1) region size by using gate C primarily[15]. The eigenvalues of the four lowest states relevant for our experiments are:

$$\begin{aligned} E_{Q_{1/2}} &= -E_Z/2 \\ E_{\Delta_{1/2}} &= -(J_{LC}+J_{RC}-\Omega+E_Z)/2 \\ E_{Q_{3/2}} &= -3E_Z/2 \\ E_{\Delta'_{1/2}} &= -(J_{LC}+J_{RC}+\Omega+E_Z)/2 \end{aligned}$$

The hyperfine interaction[16] couples the state $\Delta'_{1/2}$ to the state $Q_{3/2}(Q_{1/2})$ at their anticrossing (asymptotic approach), see Fig. 1c. ($Q_{1/2}$ and $\Delta_{1/2}$ are also hyperfine coupled.) Figure 1c also illustrates the two types of experiment we describe in this paper. With the single anticrossing (SA) pulse, based on the methodology in ref. 9, the system starts in the $\Delta'_{1/2}$ state in the (2,0,1) (or (1,0,2)) regime and then a pulse is applied to reach the (1,1,1) regime. The pulse rise time (see Supplementary Information) ensures that Landau–Zener (LZ) tunnelling creates a coherent superposition of $Q_{3/2}$ and $\Delta'_{1/2}$ on passage through the anticrossing. After a state evolution time, τ, the pulse steps down, completing the spin interferometer on the return passage through the anticrossing. The probability of the $\Delta'_{1/2}$ state occupation, $P_{\Delta'_{1/2}}$, is directly obtained by this projection back into the (2,0,1) (or (1,0,2)) regime, where the required spin-to-charge information conversion is achieved by the Pauli blockade[17] of the $Q_{3/2}$ state. An experiment with a double anticrossing (DA) pulse is also illustrated in Fig. 1c. The sequence is similar, with the important distinction that a larger pulse enables LZ tunnelling processes through both anticrossings before again projecting back in the (2,0,1) regime having passed through both anticrossings

[1]Institute for Microstructural Sciences, National Research Council Canada, Ottawa, Ontario K1A 0R6, Canada, [2]Département de physique, Université de Sherbrooke, Sherbrooke, Québec J1K 2R1, Canada. †These authors contributed equally to this work. *e-mail: Andrew.Sachrajda@nrc.ca.

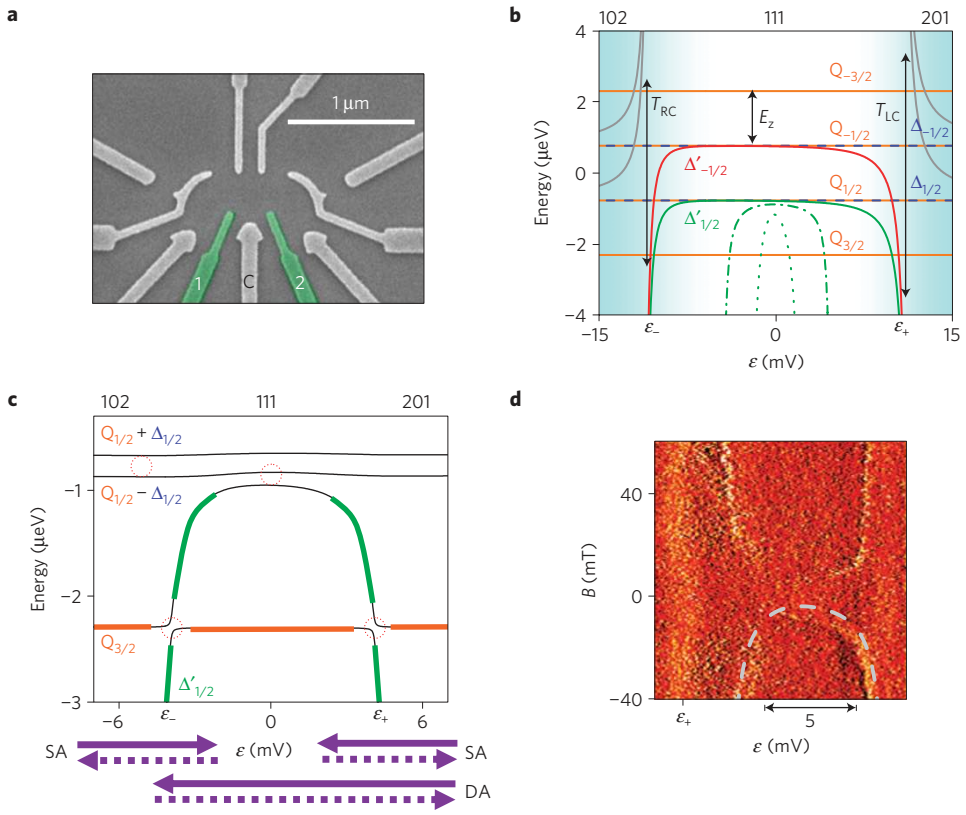

Figure 1 | Device, three-spin states spectrum, and spin arch. a, Electron micrograph of a device identical to the one measured. Gates 1 and 2 are connected to high-frequency lines for the application of fast voltage pulses (δV_1, δV_2) in addition to d.c. voltages (V_1, V_2). Gate C tunes the (1,1,1) region size by shifting the centre dot addition line. **b**, Calculated energies versus detuning ε for the three-spin states for a 22-mV-wide (1,1,1) region (that is, $|\varepsilon_+ - \varepsilon_-| = 22$ mV), neglecting the hyperfine interaction. The Zeeman splitting, E_z, originates from an applied 60 mT field. The detuning line is describing a $-45°$ angle with respect to the V_1 axis in the $V_1 - V_2$ plane. The states shown in grey are split by the tunnel couplings T_{RC} and T_{LC} (not drawn to scale) from the Δ' states. The $\Delta'_{1/2}$ state is also drawn for a midsized (1,1,1) region (green dash-dotted line) and for a narrow (1,1,1) region (green dotted curve). **c**, Calculated energy diagram including the effect of hyperfine interaction resulting from the proximity of the four lowest energy three-spin states with $S_z > 0$ (states with $S_z < 0$ are excluded for simplicity). Dotted red circles indicate pairs of states coupled by the hyperfine interaction. The dotted red circle at $\varepsilon = 0$ represents the hyperfine interaction between $\Delta'_{1/2}$ and $Q_{1/2}$ (the meaning of the remaining dotted red circles is clear). The single $\Delta'_{1/2} - Q_{3/2}$ anticrossing (SA) and double $\Delta'_{1/2} - Q_{3/2}$ anticrossing (DA) pulses are drawn. **d**, Numerical derivative of the left QPC conductance with respect to V_2 in the presence of a pulse across the charge transfer line between (2,0,1) and (1,1,1) for a 9-mV-wide (1,1,1) region . The extent of the (1,1,1) region along the detuning line (approximately joining the centres of the two charge transfer lines) is measured by a projection onto the gate voltage axis that is on the same side as the QPC detector used in the measurement. It is the resulting gate voltage range that is set equal to $|\varepsilon_+ - \varepsilon_-|$, and this is used for comparison between regimes of (1,1,1) regions with different widths. Black is low, orange is medium and yellow is high. The pulse shape is in the Supplementary Information. The detuning line makes a $-51.3°$ angle with respect to the V_1 axis in the $V_1 - V_2$ plane, permitting both sides of the spin arch to be observed. The dashed line is the theoretical fit (with detuning-dependent interdot couplings included).

twice. Important calibration information is obtained if the pulse time is longer than the coherence time (that is, $\tau > T_2^*$) where the mixing at the $\Delta'_{1/2} - Q_{3/2}$ anticrossing is detected independently of coherence effects. Figure 1d plots this against magnetic field for a 9-mV-wide (1,1,1) regime midway between the narrow and wide (1,1,1) regimes. The two anticrossings form a 'spin arch' which is used to extract the coupling parameters for the model.

The distinction between our two regimes is now clear. In the case of a wide (1,1,1) region, close to zero detuning, both J_{LC} and $J_{RC} \sim 0$, so $E_{\Delta'_{1/2}} \approx E_{\Delta_{1/2}} \approx E_{Q_{1/2}}$. Away from zero detuning only two of the spins are coupled: right–centre (left–centre) at negative (positive) detuning. Experiments using DA pulses in this regime involve coupling to not only $Q_{3/2}$ but also to $Q_{1/2}$. Thus this regime is not suitable for a two-level system involving three interacting spins. As a control experiment, however, in Fig. 2 we plot the coherent Landau–Zener–Stückelberg (LZS) oscillations obtained in this regime for both positive and negative detuning with a SA pulse. These compare to the first LZS experimental results with DQDs from ref. 9, later described theoretically in refs 18,19. The degree of LZ tunnelling, that is, the relative size of A and B in the coherent $A|\Delta'_{1/2}\rangle + Be^{i\phi(t)}|Q_{3/2}\rangle$ state, depends on the speed, v, through the anticrossing: $P_{LZ} = e^{-(2\pi\Delta^2/\hbar v)}$, where 2Δ is the energy splitting at the anticrossing. The visibility of the oscillations is a balance between this speed and T_2^*. For an infinite T_2^*, a rise time $\sim$0.2 μs would produce a 50/50 superposition (see also ref. 9). Experimentally it is found that a 6.6 ns pulse rise time (or 3.3 ns Gaussian time constant) leads to oscillations with the highest visibility. The value of T_2^*, obtained from a single parameter fit to the data, ranges from 5 to 18 ns, consistent with previous DQD experiments where T_2^* was limited by fluctuations in the nuclear field environment[1].

In Figs 3 and 4 we show results for experiments with DA pulses in a narrow (1,1,1) regime, where J_{LC} and J_{RC} are finite throughout and two well-defined qubit states exist between the two anticrossings (that is, simulations based on experimentally extracted parameters confirm that $\Delta'_{1/2}$ has moved far enough below the $Q_{1/2}$ state such that no experimental features are related to interactions with the $Q_{1/2}$ state). The energy level diagrams for this regime are shown

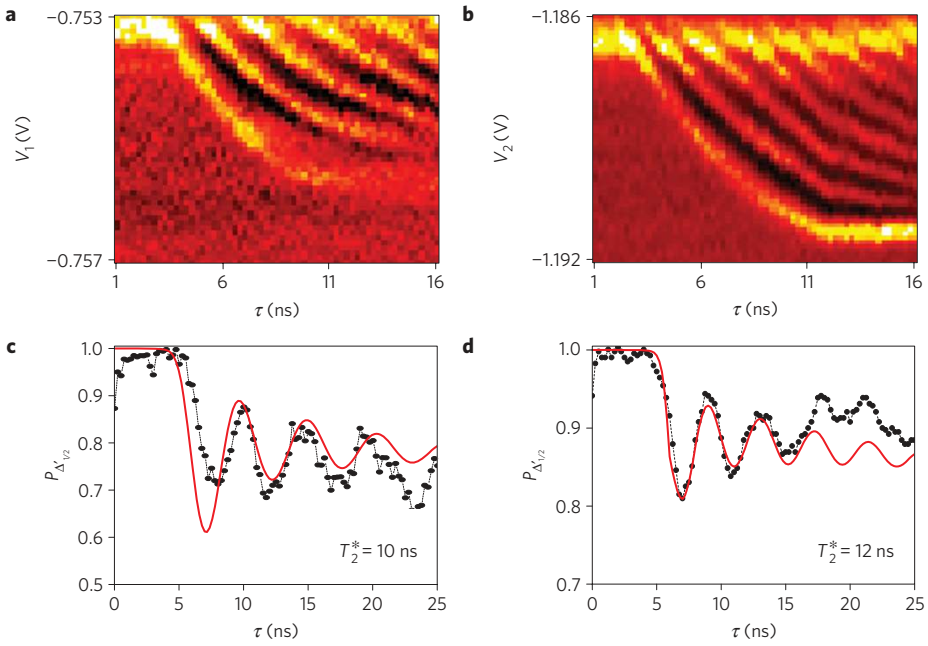

Figure 2 | LZS oscillations from the two $\Delta'_{1/2} - Q_{3/2}$ qubits for a wide (1,1,1) region. a,**b**, Numerical derivative of the conductance with respect to detuning showing LZS oscillations versus pulse duration τ. Black is low, red is medium and yellow is high. Panel **a** shows measurements with the right QPC for $|\varepsilon_+ - \varepsilon_-| = 27$ mV along V_1; the pulse goes across the (1,0,2) to (1,1,1) charge transfer line at $B = 60$ mT. Both V_2 and V_1 are swept to detune parallel to the pulse direction in the $V_1 - V_2$ plane. Panel **b** shows measurements with the left QPC for $|\varepsilon_+ - \varepsilon_-| = 41.5$ mV along V_2; the pulse goes across the (2,0,1) to (1,1,1) charge transfer line at $B = 60$ mT. **c**,**d**, Probability of ending in the $\Delta'_{1/2}$ state as a function of τ with fits for T_2^*. For the right QPC (**c**) the pulse goes from (1,0,2) to (1,1,1) and $|\varepsilon_+ - \varepsilon_-| \sim 50$ mV along V_1. For the left QPC (**d**) the pulse goes from (2,0,1) to (1,1,1) and $|\varepsilon_+ - \varepsilon_-| = 27$ mV along V_2. The experimental data are shown as points, whereas the theoretical fits are shown as red lines. The values of T_2^* extracted from the single parameter fit to the LZS model are indicated.

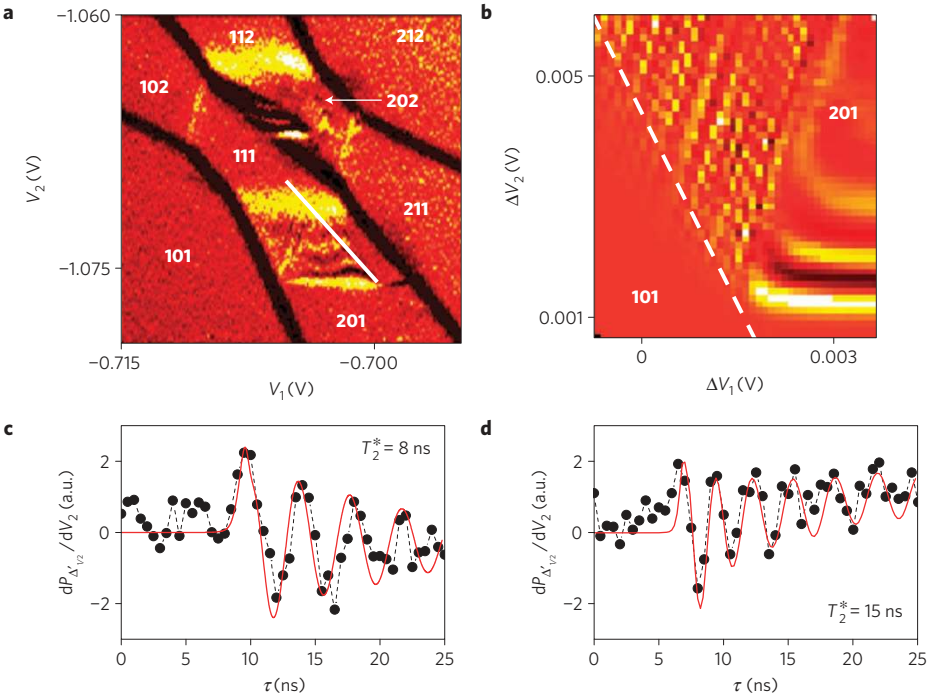

Figure 3 | Coherent three-spin state manipulation with a narrow (1,1,1) region a, Stability diagram in the presence of a pulse (drawn as a white line for a given (V_1, V_2)), showing coherent LZS oscillations in the (2,0,1) region with features parallel to both charge transfer lines. The colour map (black is low, red is medium and yellow is high) corresponds to the numerical derivative of the left QPC conductance with respect to V_2 in the presence of a pulse across the charge transfer line between (2,0,1) and (1,1,1). The (1,1,1) region is tuned to a width of ~5 mV with gate C. $B = 25$ mT. The stability diagram also shows LZS oscillations involving (2,0,2) and (1,1,2). **b**, Calculated $dP_{\Delta'_{1/2}}/dV_2$ map zooming mainly into the (2,0,1) region of the stability diagram from **a**. The dashed line shows where the addition line is expected, although it is not part of the calculation. $B = 40$ mT. **c**,**d**, Traces of $dP_{\Delta'_{1/2}}/dV_2$ versus τ. For **c** the data points are extracted from Fig. 4b (40 mT, white line) at $V_2 = -1.0,751$ V. For **d** the data points are extracted from Fig. 4b (40 mT, blue line) at $V_2 = -1.074$ V. The fits (red lines) use $B = 60$ mT. The values of T_2^* extracted from the fits are indicated.

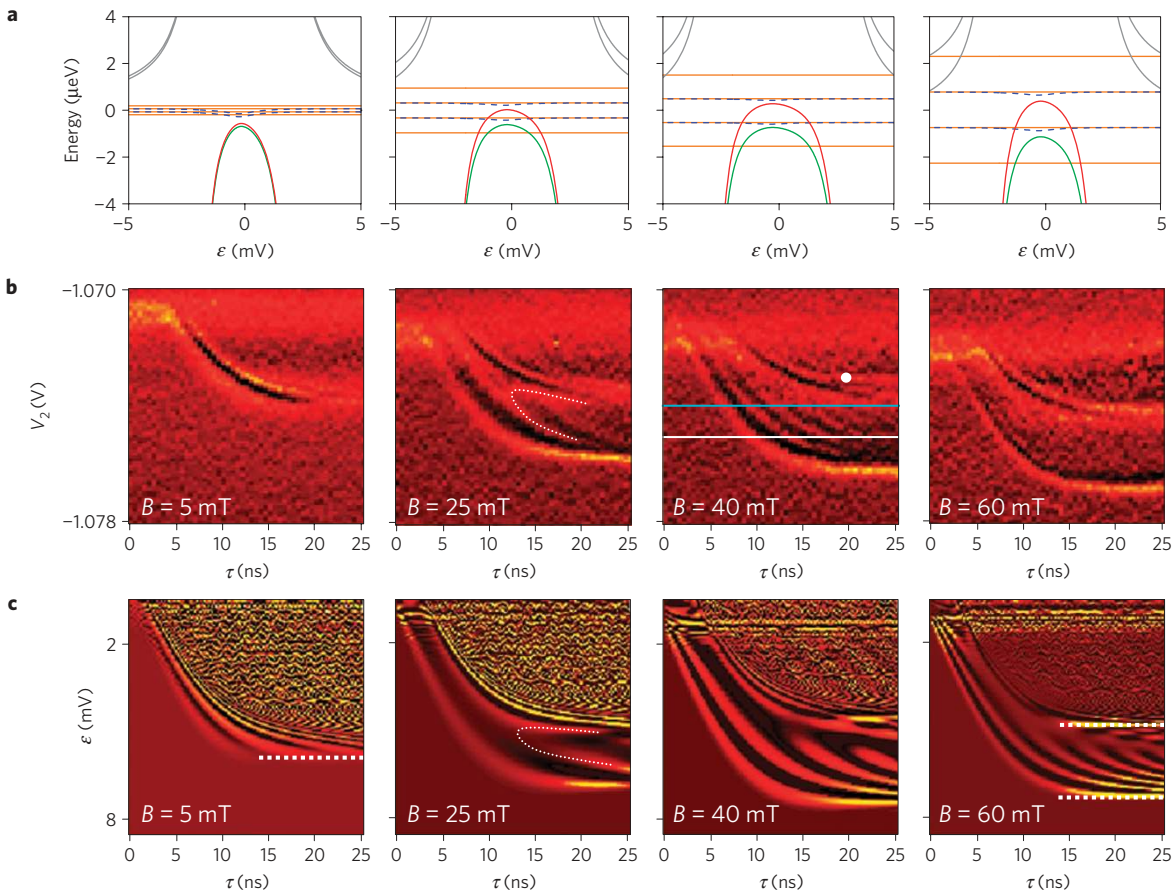

Figure 4 | Magnetic field dependence of coherent three-spin state manipulation with a narrow (1,1,1) region. a, Energy spectra for the three-spin states for different magnetic fields. The colour code for the states is the same as in Fig. 1b. From left to right we have: $B = 5$ mT and $|\varepsilon_+ - \varepsilon_-| = 3.9$ mV; $B = 25$ mT and $|\varepsilon_+ - \varepsilon_-| = 5.1$ mV; $B = 40$ mT and $|\varepsilon_+ - \varepsilon_-| = 5.6$ mV; and $B = 60$ mT and $|\varepsilon_+ - \varepsilon_-| = 4.6$ mV. **b**, Coherent oscillations shown in the $\tau - V_2$ plane as the numerical derivative of the left QPC conductance with respect to V_2 (black is low, red is medium and yellow is high) in the presence of a pulse across the charge transfer line between (2,0,1) and (1,1,1). The (1,1,1) region is tuned to a width of ~5 mV with gate C. V_1 is swept proportionally to V_2 to detune parallel to the pulse direction. The magnetic field and (1,1,1) region sizes from left to right are as in **a**. The white dot in the $B = 40$ mT map indicates a coherent oscillation resulting from a DA pulse reaching past the far $\Delta'_{1/2} - Q_{3/2}$ anticrossing. **c**, Calculated $dP_{\Delta'_{1/2}}/dV_2$ maps (black is low, red is medium and yellow is high) in the $\tau - \varepsilon$ plane for the same experimental settings as for **b**. The magnetic field and (1,1,1) region sizes from left to right are as in **a**. To keep the fringes clearer, dephasing is not included. The very rapid oscillations in the upper right corner of the figures are an artefact due to the large exchange energy past the far $\Delta'_{1/2} - Q_{3/2}$ anticrossing. At $B = 5$ mT, the anticrossings have merged, so there is only one boundary in the diagram (white dashed line). At $B = 60$ mT, two $\Delta'_{1/2} - Q_{3/2}$ anticrossings are recovered (see the two white dashed lines). At $B = 25$ mT, for both theory and experiment, dotted white curves are drawn as a guide to the eye for the peak of an oscillation in between the two $\Delta'_{1/2} - Q_{3/2}$ anticrossings. We note that a small DNP effect[20] is present which depends on the size of the (1,1,1) region, details of pulse shape and pulse orientation. In **b**,**c** (25 and 40 mT), it is found that a DNP ~20 mT is required to properly describe the period of oscillations. This is why the stability diagram in Fig. 3b is calculated at 40 mT rather than 25 mT, and why the fits in Fig. 3c,d are calculated at 60 mT instead of 40 mT.

in Fig. 4a. The stability diagram, measured in the presence of a fixed amplitude DA pulse at 25 mT, is shown in Fig. 3a. The results reveal LZS resonances parallel to both charge transfer lines, consistent with theoretical simulations (Fig. 3b) and confirming that coherence is maintained as the $\Delta'_{1/2}$ state is transformed from one dominated by coupling between left and centre spins to one dominated by right and centre spins, effectively demonstrating coherent pairwise exchange control.

To gain further insight, Fig. 4b and c show experimental and theoretical plots of the pulse duration dependence of LZS oscillations at different magnetic fields. Two boundaries, marked with horizontal white dashed lines, can be observed at fields above 25 mT. The region between the boundaries corresponds to the regime between the two anticrossings, while the resonances correspond to LZS oscillations. It can be seen (for example, curved dotted lines) that the resonances double back on themselves. This is a direct observation of tracking the resonance across the maximum in the $\Delta'_{1/2}$ versus detuning curve (see Figs 4a and 1b). We speculate that operating at this spot may provide more protection from charge noise, as the energy levels become locally flat versus detuning.

Although the frequency of coherent oscillations grows with field, owing to the increased spacing between the two qubit levels, it seems as if the experiment and theory differ by 20 mT for experimental data at 40 mT and by 15 mT for data at 25 mT. We attribute this to a dynamic nuclear polarization effect (DNP; ref. 20). To make this quantitative we extract horizontal slices in Fig. 4b at 40 mT (blue and white lines) and fit them to obtain T_2^*. The data are consistent with a 20 mT DNP effect. It is found experimentally that the values of T_2^* for the three-spin qubit experiments in Fig. 3c,d (8–15 ns) are within error identical to the values from the two-spin qubit experiments. This is consistent with T_2^* being dominated by local uncorrelated nuclear field fluctuations as both sets of qubit states differ by the same total spin[21]. Finally, we note that we also observe a resonance beyond the second anticrossing,

marked with a white spot in Fig. 4b. This is a non-trivial feature corresponding to a resonance condition of two interacting spin interferometers, one between the two anticrossings and a second, beyond the second anticrossing.

In conclusion, we have demonstrated coherent control of a qubit based on three-interacting-spin states. We have confirmed that there is no detectable change in the coherence time in the three-spin experiments compared with the two-spin experiments. We have realized the pairwise control of exchange for a three-spin system by pulsing the detuning energy of a triple quantum dot. The same technique should carry over when more quantum dots are added in series to increase the number of qubits. Pairwise control of exchange, as demonstrated here, will then be useful for building complex quantum algorithms based on electron spin qubits in quantum dots.

Received 16 June 2011; accepted 21 October 2011; published online 27 November 2011

References

1. Petta, J. R. *et al.* Coherent manipulation of coupled electron spins in semiconductor quantum dots. *Science* **309,** 2180–2184 (2005).
2. Koppens, F. H. L. *et al.* Driven coherent oscillations of a single electron spin in a quantum dot. *Nature* **442,** 766–771 (2006).
3. Hanson, R., Kouwenhoven, L. P., Petta, J. R., Tarucha, S. & Vandersypen, L. M. K. Spins in few-electron quantum dots. *Rev. Mod. Phys.* **79,** 1217–1265 (2007).
4. Pioro-Ladrière, M. *et al.* Electrically driven single-electron spin resonance in a slanting Zeeman field. *Nature Phys.* **4,** 776–779 (2008).
5. DiVincenzo, D. P., Bacon, D., Kempe, J., Burkard, G & Whaley, K. B. Universal quantum computation with the exchange interaction. *Nature* **408,** 339–342 (2000).
6. Greentree, A. D., Cole, J. H., Hamilton, A. R. & Hollenberg, L. C. L. Coherent electronic transfer in quantum dot systems using adiabatic passage. *Phys. Rev. B* **70,** 235317 (2004).
7. Shevchenko, S., Ashhab, S. & Nori, F. Landau–Zener–Stückelberg interferometry. *Phys. Rep.* **492,** 1–30 (2010).
8. Zener, C. Non-adiabatic crossing of energy levels. *Proc. R. Soc. Lond. A* **137,** 696–702 (1932).
9. Petta, J. R., Lu, H. & Gossard, A. C. A coherent beam splitter for electronic spin states. *Science* **327,** 669–672 (2010).
10. Loss, D. & DiVincenzo, D. P. Quantum computation with quantum dots. *Phys. Rev. A* **57,** 120–126 (1998).
11. Ciorga, M. *et al.* Addition spectrum of a lateral dot from Coulomb and spin-blockade spectroscopy. *Phys. Rev. B* **61,** R16315–R16318 (2000).
12. Elzermann, J. *et al.* Few-electron quantum dot circuit with integrated charge read out. *Phys. Rev. B* **67,** 161308(R) (2003).
13. Field, M. *et al.* Measurements of Coulomb blockade with a noninvasive voltage probe. *Phys. Rev. Lett.* **70,** 1311–1314 (1993).
14. Laird, E. A. *et al.* Coherent spin manipulation in an exchange-only qubit. *Phys. Rev. B* **82,** 075403 (2010).
15. Granger, G. *et al.* Three-dimensional transport diagram of a triple quantum dot. *Phys. Rev. B* **82,** 075304 (2010).
16. Taylor, J. M. *et al.* Relaxation, dephasing, and quantum control of electron spins in double quantum dots. *Phys. Rev. B* **76,** 035315 (2007).
17. Ono, K., Austing, D. G., Tokura, Y. & Tarucha, S. Current rectification by Pauli exclusion in a weakly coupled double quantum dot system. *Science* **297,** 1313–1317 (2002).
18. Ribeiro, H., Petta, J. R. & Burkard, G. Harnessing the GaAs quantum dot nuclear spin bath for quantum control. *Phys. Rev. B* **82,** 115445 (2010).
19. Särkkä, J. & Harju, A. Spin dynamics at the singlet–triplet crossings in a double quantum dot. *New J. Phys.* **13,** 043010 (2011).
20. Brataas, A. & Rashba, E. Nuclear dynamics during Landau–Zener singlet–triplet transitions in double quantum dots. *Phys. Rev. B* **84,** 045301 (2011).
21. Baugh, J. *et al.* Solid-state NMR three-qubit homonuclear system for quantum-information processing: Control and characterization. *Phys. Rev. A* **73,** 022305 (2006).

Acknowledgements

We thank D. G. Austing, W. Coish and E. Laird for discussions and O. Kodra for programming. A.S.S. and M.P-L. acknowledge funding from NSERC. G.G., A.K, M.P-L., and A.S.S. acknowledge funding from CIFAR. G.G. acknowledges funding from the NRC-CNRS collaboration.

Author contributions

Z.R.W. developed and grew the 2DEG heterostructure free of telegraphic noise; A.K. fabricated the triple quantum dot device capable of reaching the few-electron regime; P.Z., L.G. and S.A.S. designed and built the high-frequency lines up to 50 GHz at millikelvin temperatures; P.Z., L.G. and G.G. ran the cryogenic equipment; L.G., G.G., S.A.S. and M.P-L. developed the pulsing techniques; G.G., L.G. and S.A.S. performed the measurements; G.G., L.G. and G.C.A. analysed the data; G.C.A. performed theoretical simulations; G.G. and A.S.S. wrote the manuscript and Supplementary Information with input from all authors; G.G., L.G. and G.C.A made the figures; G.G., L.G., G.C.A., S.A.S., M.P-L. and A.S.S. participated in discussions concerning the experimental and theoretical results; and A.S.S. supervised the project.

Additional information

The authors declare no competing financial interests. Supplementary information accompanies this paper on www.nature.com/naturephysics. Reprints and permissions information is available online at http://www.nature.com/reprints. Correspondence and requests for materials should be addressed to A.S.S.